# Total Surface Current Vector and Shear from a Sequence of Satellite images: Effect of Waves in Opposite Directions

Fabrice Ardhuin[1], Matias Alday[2], and Maria V. Yurovskaya[3]

[1]Univ. Brest, CNRS, Ifremer, IRD
[2]CNRS, Ifremer
[3]Marine Hydrophysical Institute

November 22, 2022

**Abstract**

The Total Surface Current Velocity (TSCV) - the horizontal vector quantity that advects seawater - is an Essential Climate Variable, with few observations available today. The TSCV can be derived from the phase speed of surface gravity waves, and the estimates of the phase speeds of different wavelengths could give a measure of the vertical shear. Here we combine 10-m resolution Level-1C of the Sentinel 2 Multispectral Instrument, acquired with time lags up to 1s, and numerical simulation of these images. Retrieving the near surface shear requires a specific attention to waves in opposing direction when estimating a single phase speed from the phase difference in an image pair. Opposing waves lead to errors in phase speeds that are most frequent for shorter wavelengths. We propose an alternative method using a least-square fit of the current speed and amplitudes of waves in opposing directions to the observed complex amplitudes of a sequence of 3 images. When applied to Sentinel 2, this method generally provides more moisy estimate of the current. A byproduct of this analysis is the "opposition spectrum" that is a key quantity in the sources of microseisms and microbaroms. For future possible sensors, the retrieval of TSCV and shear can benefit from increased time lags, resolution and exposure time of acquisition. These findings should allow new investigations of near-surface ocean processes including regions of freshwater influence or internal waves, using existing satellite missions such as Sentinel 2, and provide a basis for the design of future optical instruments.

# Total Surface Current Vector and Shear from a Sequence of Satellite images: Effect of Waves in Opposite Directions

**Fabrice Ardhuin**[1,2] **and Matias Alday**[1]

**Maria Yurovskaya**[3,4]

[1]Univ. Brest, CNRS, Ifremer, IRD, Laboratoire d'Océanographie Physique et Spatiale, Brest, France
[2]Scripps Institution of Oceanography, University of California San Diego, La Jolla, California
[3]Marine Hydrophysical Institute of RAS, Sevastopol, Russia
[4]Russian State Hydrometeorological Institute, St. Petersburg, Russia

## Key Points:

- Phase shifts in lagged pairs of satellite images yield information on near surface current and shear
- Waves in opposite directions can corrupt current estimates in particular for wavelengths under 25 m
- A sequence of 3 images gives a separation of waves in opposing direction and a current estimate

Corresponding author: Fabrice Ardhuin, ardhuin@ifremer.fr

## Abstract

The Total Surface Current Velocity (TSCV) - the horizontal vector quantity that advects seawater - is an Essential Climate Variable, with few observations available today. The TSCV can be derived from the phase speed of surface gravity waves, and the estimates of the phase speeds of different wavelengths could give a measure of the vertical shear. Here we combine 10-m resolution Level-1C of the Sentinel 2 Multispectral Instrument, acquired with time lags up to 1s, and numerical simulation of these images. Retrieving the near surface shear requires a specific attention to waves in opposing direction when estimating a single phase speed from the phase difference in an image pair. Opposing waves lead to errors in phase speeds that are most frequent for shorter wavelengths. We propose an alternative method using a least-square fit of the current speed and amplitudes of waves in opposing directions to the observed complex amplitudes of a sequence of 3 images. When applied to Sentinel 2, this method generally provides more moisy estimate of the current. A byproduct of this analysis is the "opposition spectrum" that is a key quantity in the sources of microseisms and microbaroms. For future possible sensors, the retrieval of TSCV and shear can benefit from increased time lags, resolution and exposure time of acquisition. These findings should allow new investigations of near-surface ocean processes including regions of freshwater influence or internal waves, using existing satellite missions such as Sentinel 2, and provide a basis for the design of future optical instruments.



## Plain Language Summary

Measuring ocean surface current and its vertical variation is important for a wide range of science questions and applications. A well known technique for measuring currents from ocean surface images is to follow the motion of wave crests from one image to another, measuring their celerity. The values obtained for different wavelenghts gives access to an estimate of the current at different depths. When using only two images, the technique breaks down if there are waves travelling in opposing directions with comparable energy levels. Here we generalize the technique to a sequence of 3 images that allows to separate the waves in opposing directions. We show that this is an important improvement for measuring the celerity of the shorter wave components because there are generally waves in opposing directions with significant energy for wavelengths shorter than 25 m. Applications of the method to existing data from the Sentinel 2 satellite is difficult due to short time differences between image acquisitions. Several improvements on the Sentinel 2 sensor are proposed for a specific instrument that would measure surface current and shear.


## 1 Introduction

Surface current velocities play an important role in many ocean processes, including the flux of kinetic energy from the atmosphere to the ocean (Wunsch & Ferrari, 2009), air-sea fluxes (Cronin et al., 2019), and the transport of buoyant material (Maximenko et al., 2019). Different observation systems have been proposed to measure the surface current in a wide range of conditions. Barrick (1977) and many others have developed land-based HF radars that rely on the dispersion relation of surface gravity waves, while open ocean conditions are very sparsely monitored by a wide range of techniques that differ in their effective depth of measurement, as illustrated in Fig. 1. In situ moorings are typically limited to measurements at depths larger than 5 m, away from the layer where the Stokes drift of surface gravity waves is strong. In particular, Surface Velocity Program (SVP) drifters have been designed to have the least influence of wave motions in their measurements thanks to a drogue centered around 15 m depth (Niiler & Paduan, 1995; Lumpkin et al., 2017). In the absence of that drogue, the drifter measures a not so clear combination of wind and surface current speeds (Elipot et al., 2016). The surface drifts of Argo floats have also been used (Lebedev et al., 2007), and, for the lack of a better alternative, satellite remote sensing can be used, combining scatterometer winds, sea level anomalies from altimeters, and a combination of drifters and satellite gravimeters for the Mean Dynamic Topography (Rio et al., 2014).

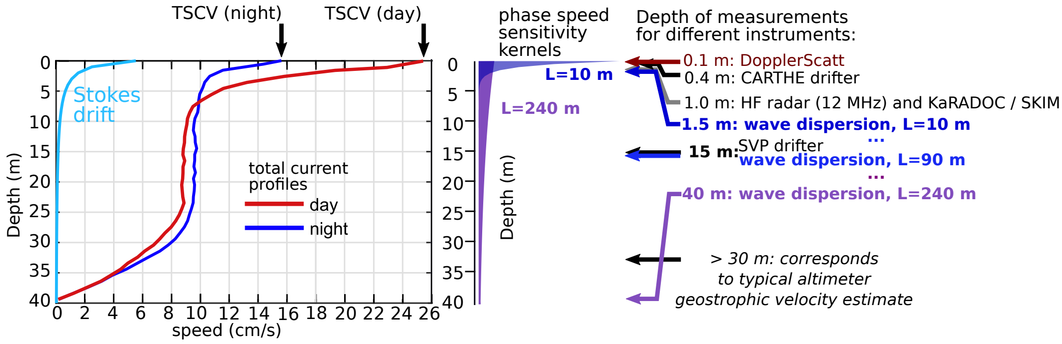


**Figure 1.** Left: typical day and night velocity profiles of the total current in the Atlantic at 26N , 36W (adapted from Sutherland et al. 2016). Center: sensitivity kernels for surface gravity wave phase speeds. Right: depth of measurement of different instruments. From top to bottom: DopplerScatt (Rodríguez et al., 2018), CARTHE drifters (Novelli et al., 2017), HF radars at 12 MHz (Stewart & Joy, 1974), near nadir Ka-band radars such as KaRADOC (Marié et al., 2020).

These estimates of the near-surface current can have significant differences, in part due to the sampling of different depths as illustrated in Fig. 1. Each measurement system provides a horizontal current velocity that is a convolution of the vertical profile of the velocity. For simplicity, it is convenient to define a "measurement depth" that can be taken at the depth at which a linearly varying current takes the given value. We note that DopplerScatt involves an empirical Geophysical Model Function and thus the physics of the measurement are not completely understood but the backscatter dominated by short gravity waves suggests a measurement depth under 0.1 m, whereas near-nadir radar measurements, such as performed by the KaRADOC instrument (Marié et al., 2020) give a velocity that is weighted by the surface slope spectrum and corresponds to a measurement depth does not vary much around 1 m depth. It is thus desirable to measure the vertical shear of the current in order to be able to compare or combine these estimates. The shear is also an important indication of mixing or lack thereof, giving information on possible upper ocean stratification.

Shear estimates have used the wave dispersion modification due to the current vector, defined by the two components $U_x(z)$ and $U_y(z)$ of the horizontal current profile (Stewart & Joy, 1974). For completeness, a non-linear wave correction should also be included (Broche et al., 1983; Ardhuin et al., 2009), which is almost the same as replacing the Eulerian mean current by the Lagrangian mean current (Andrews & McIntyre, 1978). We thus expect, for $kD \gg 1$,

$$U(k, \varphi) \simeq U(k) \cos(\varphi - \varphi_U) = \int_{-D}^{0} U_x(z) \exp(2kz) \mathrm{d}z \cos\varphi + \int_{-D}^{0} U_y(z) \exp(2kz) \mathrm{d}z \sin\varphi. \tag{1}$$

Obtaining current shear from a sequence of images has been done from many sensors including stereo-video imagery (Fedele et al., 2013), X-band radar (Campana et al., 2016) or polarimetric imagery (Laxague et al., 2018). In all cases it requires reliable estimates of $U(k, \varphi)$, for different wavelengths, including the shortest components, and this is performed by identifying propagating waves in the three-dimensional (3D) Fourier transform of the measured signals (Young et al., 1985; Peureux et al., 2018). A great opportunity is offered by satellite imagery with accurately co-registered views of the same ocean surface with short time lags. This is particularly the case of Sentinel 2 imagery has been used to estimate surface current (Kudryavtsev et al., 2017b). The Sentinel 2 Multispectral Instrument (Drusch et al., 2012) has very strict co-registration requirements that make it possible to observe the signature of current velocities of the order of 1 m/s (Yurovskaya et al., 2018). Compared to methods that use a series of many images processed with a 3D Fourier transform, the analysis of only a few images is more difficult because of the very poor temporal resolution that does not give a full spectrum in the frequency domain. In particular the linear wave signal is not so easily separated from other contributions to the measurement.

The objective of the present paper is to discuss the influence of this limited time sampling on the accuracy of surface current estimates, in the presence of waves propagating in opposing directions, starting with the 2-image method used by Kudryavtsev et al. (2017b), as discussed in Section 2. In order to demonstrate the different processing steps and the influence of the image properties, we rely on the comparison of true data and simulated images generated using the simulator described in Appendix A. Due to the possible corruption of phase speeds by waves in opposing directions, we propose a new method using sequences of 3 images, as described in Section 3 with details given in Appendix B. Discussions and conclusions follow in Sections 4 and 5. This paper does not address issues associated to systematic errors in the spatial registration on a global reference system with sub-pixel accuracy. These are partly discussed in Kääb et al. (2016) and Yurovskaya et al. (2019) and will be the topic of future work.

## 2 Effect of waves in opposite directions with 2-image sun glint method

### 2.1 Short waves in opposing directions

Pictures of the sun glint reveal wave patterns that are caused by the tilting of the sea surface by waves with wavelength larger than the pixel, adding their long wave slope to the local slope probability density function, and thus changing the pixel brightness. This effect has been described in many papers including Kudryavtsev et al. (2017a), and the geometry of the measurement is defined in Fig. 2. A key concept is that the surface can be decomposed in facets with a size of the order of 1 mm by 1 mm, scale at which the sea surface is well approximated by a plane. There are thus a large number of such facets in a typical image pixel (10 m by 10 m for some of the bands of the MSI sensor on Sentinel 2) but the number of those that correspond to the specular direction can be relatively small, of the order of 100, while their brightness also varies, introducing random fluctuations in the image brightness.

As shown in Fig. 2.b for a spherical Earth, the satellite position S and observation point O correspond to a zenithal angle $\theta_v$, related to the off-nadir angle $\gamma$ by the law of sines,

$$\sin\gamma/R_E = \sin(\pi - \theta_v)/(R_E + H). \tag{2}$$

Because the time of acquisition of the different pixels is not available in the Level-1C Sentinel 2 product, it can be retrieved from the provided view geometry. For example color band B01 is acquired at time $t_1$ when B02 is acquired at time $t_2$, the time difference is given by the ratio of the angular distance $\alpha_{1,2}$ between the two nadir points $N_1$ and $N_2$, as depicted in Fig. 2.c, and the angular speed along the orbit $\Omega$ (in rad/s). The angular distance $\alpha_{1,2}$ is obtained from the law of cosines on the sphere,

$$\cos\alpha_{1,2} = \cos\alpha_1 \cos\alpha_2 + \sin\alpha_1 \sin\alpha_2 \cos(\varphi_2 - \varphi_1). \tag{3}$$

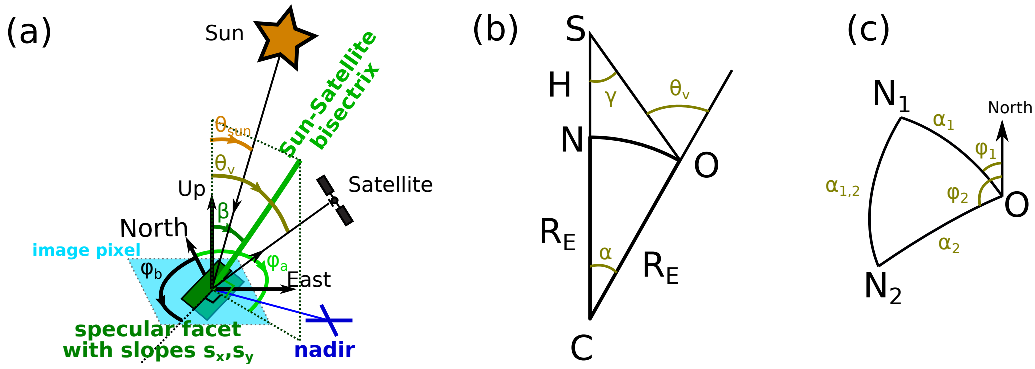


**Figure 2.** (a) Definition of viewing angles corresponding to a given sun and satellite sensor positions. The image brightness of a pixel is defined by the area of sub-pixel facets (in green) that gives a specular reflection and thus must have a given surface slope vector $(s_x, s_y)$. That area is proportional to the probability density function within that pixel for the slope $(s_x, s_y)$. This slope corresponds to the zenith angle $\beta$ and azimuth $\varphi_a$. The perpendicular azimuths $\varphi_b = \varphi_a \pm \pi/2$ are "blind azimuths" in which the waves contribute a second order change to the pixel brightness and cannot be observed. (b) Position of satellite (S), observation point (O) and center of the Earth (C) in a vertical plane. (c) Triangle on the sphere joining the observation point O and the nadir positions $N_1$ and $N_2$ at observation times 1 and 2.

This typically gives distances and time lags within 1% of the expression given by eq. (1) in Yurovskaya et al. (2019).

In order to illustrate the limitations of the 2-image method, we start from the same image example that was used in Kudryavtsev et al. (2017a), acquired off the California coast in the region of San Diego. The image processing method is illustrated in Fig. 3. In order to understand the processing results, we also have generated simulated images and applied the exact same processing to the them.

The image simulator is described in more detail in Appendix A, and corresponds to the forward model of Kudryavtsev et al. (2017a), combined with a noise model. For our first example, the model input parameters are the Sentinel 2 viewing geometry, an estimate of the surface wind vector given by satellite scatterometer data, and a directional wave spectrum that is estimated from an in situ buoy. The buoy is station number 220 of the Coastal Data Information Program (CDIP) located at 32.752N 117.501W, also identified by the World Meteorological Organization with the number 46258.

In order to obtain a more robust estimation of the current speed, we used a phase estimated from the coherent sum of the complex amplitudes obtained from individual image tiles that are 500 m wide. We first sum the $16^2$=256 tiles, and then add $15^2$ tiles that are shifted by 250 m in each direction in order to use the signal that is otherwise much reduced by the 2-dimensional Hann window. This gives 512 degrees of freedom for each spectral estimate.

The shortest waves that propagate along the $x$ or the $y$ axis in the image have a 20 m wavelength. Their phase speed, for zero current, is expected to be 5.6 m/s and they should be displaced by 0.6 m between the red and the blue channels that are separated by 1.0 s, and only 0.3 m between the red and green. This distance is much smaller than the 10 m pixel size, and smaller than the requirement for co-registration of the MSI sensor set to 3 m for 3 standard deviations (Drusch et al., 2012). However, this is easily picked

Figure 3. Example of processing from Level-1C images to phase speeds, using 500 x 500 m tiles over a 8 by 8 km area, giving 512 degrees of freedom. Top: data from Copernicus Sentinel 2 on 29 April 2016 off California (See Figs. 3-9 in Kudryavtsev et al. 2017), with $= 9$, $U_{10} = 6$ m/s. Bottom: simulated S2 data based on *in situ* wave spectrum determined from directional moments using the Maximum Entropy Method, and with random phases. The multiplicative noise amplitude is set to $N_t = 0.15$. The present paper was motivated by the phase speed anomalies, highlighted with the dashed magenta circle near the Nyquist wavelength $L = 20$ m.

up by Fourier analysis. In fact, Fig. 3 shows that the phase speeds down to 25 m wavelength are consistent with linear wave theory. However, between 25 m and 20 m waves large fluctuations of the order of 1 m/s are found, and these vary strongly with the choice of azimuth $\varphi$. Such fluctuations are not included in the surface current estimates made by Yurovskaya et al. (2019), because these authors exclude spectral components with a coherence under 0.8. This coherence, denoted "coh" in the following equations and figures, is also called magnitude-squared coherence. We note that this threshold is equivalent to a standard deviation of the co-spectrum phase of 40°, because for small values of the phase $\psi$ in radians, $\mathrm{std}(\psi) \simeq 2\sqrt{1 - \mathrm{coh}}$.

However, if the vertical shear in the top few meters is to be measured, we have to use these shorter wave components. Presumably we could use spectral components with a lower coherence, hence a larger uncertainty, and use the averaging over a larger number of spectral components to mitigate this larger uncertainty. For the shorter components, with $k \simeq 40$ cpkm, the coherence is under 0.35 for all directions, and highest for $110° < \varphi < 120°$, with a corresponding fluctuation of the phase $\mathrm{std}(\psi) \simeq 70°$. Interestingly, the same low coherence and high level of phase fluctuation are also present in the simulated data, even when the noise level is reduced to zero. We found that this pattern was not associated to the amplitude or the additive or multiplicative nature of the noise in eq. (A1), as long as some energy remains for waves in opposing directions. These fluctuations in the phase speed for the shortest wave components disappear in the simulation when the input spectrum is "chopped" to remove waves propagating from the east (with $k_x < 0$, see Fig. 4). Clearly, the spurious large values of phase speeds for wavelengths $20\,\mathrm{m} < L < 25$ m are associated to a significant level of energy in opposing directions.

Any spectral component $(k, \varphi)$ contains information that propagate in both directions $\varphi$ and $\varphi + \pi$. By interpreting the phase difference $\psi_{4,2}$ as the phase of a single travelling wave, in direction $\varphi$ if the phase speed is positive, we are assuming that we can neglect the waves in the opposite direction. In fact, the data is in general the sum of two rent to the value estimated from the phase method and only fit $Z_A$ and $Z_B$, in that case the values of $H$ are more realistic, as shown in Fig. 9.e. For that estimate we have also modified the equations in Appendix B to allow for a different current at times $t_2$ and $t_3$ in order to absorb the biases in the image position $(\delta X, \delta Y)_{i,j} = (U_{ij}, V_{ij})(t_j - t_i)$. Indeed the phase difference $\psi_{2,3}$ gives a velocity vector close to (-1.8,0.) while $\psi_{2,4}$ gives (-1.,0) corresponding to a 1 m eastward erroneous shift of the B02 image relative to B03 and B04. This inconsistency in the data is not included in the fitted model proposed in Appendix B and thus contributes to higher errors in the estimate of $U$. One possibility may be to recompute the least squares with different velocities over the different time lags, or to use the phase difference method on all image pairs to estimate deviations from a constant speed and shift the image before applying the least square method.

For our test image, it is thus dubious that the least-square method, as implemented here, has provided any additional reliable information for short waves compared to the phase method. Using a more conservative threshold $\varepsilon_r < 0.2$ it is possibly able to slightly extend the part of the spectral plane from which a velocity can be derived to directions that are further away from the mean wave direction.

Looking beyond the particular case of the bands B02, B03 and B04 of the Sentinel 2 sensor, it is interesting to know how well this method may work, for example on the future Sentinel 2 Next Generation or on the optical instrument proposed for STREAM. We have thus simulated the image and its processing, and reduced the noise level from $N_t = 0.15$ (which looks similar to the true S2 image) to no noise at all with $N_t = 0$. Without any noise, the least square fit is very good with $\varepsilon_r < 0.1$ for the full spectral domain, except around the blind azimuth. As a result the input current vector $\mathbf{U} = (-1, 0)$ m/s is very well recovered. This would not be the case for the shortest components using the phase method except in the mean direction, giving only one component of the current vector.

The precision on the retrieval of the surface current is further illustrated in Figure 10, focusing on a narrow range of azimuths, between 110 and 120°. The error bars give an estimate of the precision of the mean within each spectral bin that are all completely independent. For the phase-difference method, the smooth variation of the estimates across the spectra (within the error bar) confirm that the O(15 cm/s) precision for each spectra estimate is realistic. This does not say anything about the accuracy of the estimate that is dominated by an O(1 m/s) error due to relative pixel co-registration errors of the different bands.

For the least-square methods, the error bars are more difficult to define given the heavy tails of the $U$ distribution and the sample size (256 independent spectra giving 256 degrees of freedom for $U$). It might be possible to use the distribution of residuals $\varepsilon_m$ obtained for the $M$ spectra as given by eq. (5), because they are correlated with errors on $U$, but we have not found a satisfactory parameterization that would work for both the academic 1D case of Figure 8 and the true images. If needed, the only robust uncertainty we can propose is to compute the standard deviation across neighboring spectral components, for example in a 10 cpkm band of wavenumbers. Both the phase and least square methods agree in the range 25 cpkm to 35 cpkm but there are large biases of the least-square method for both short and long components as shown in Fig. 10.a. Although some of these errors could be caused by instrument errors (such as errors in the retrieved observation angles that could change the estimate time lags and distort the dispersion relation), it is striking that the simulated data shown in Fig. 10.b gives similar errors, but slightly weaker, which leads us to think that the biases in the least square method may be dominated by artefacts of the processing method. We have not yet identified the source of these errors. We also note that the phase method, in contrast, has no trend in the simulated data for which the standard deviation of the phase is under 60°.

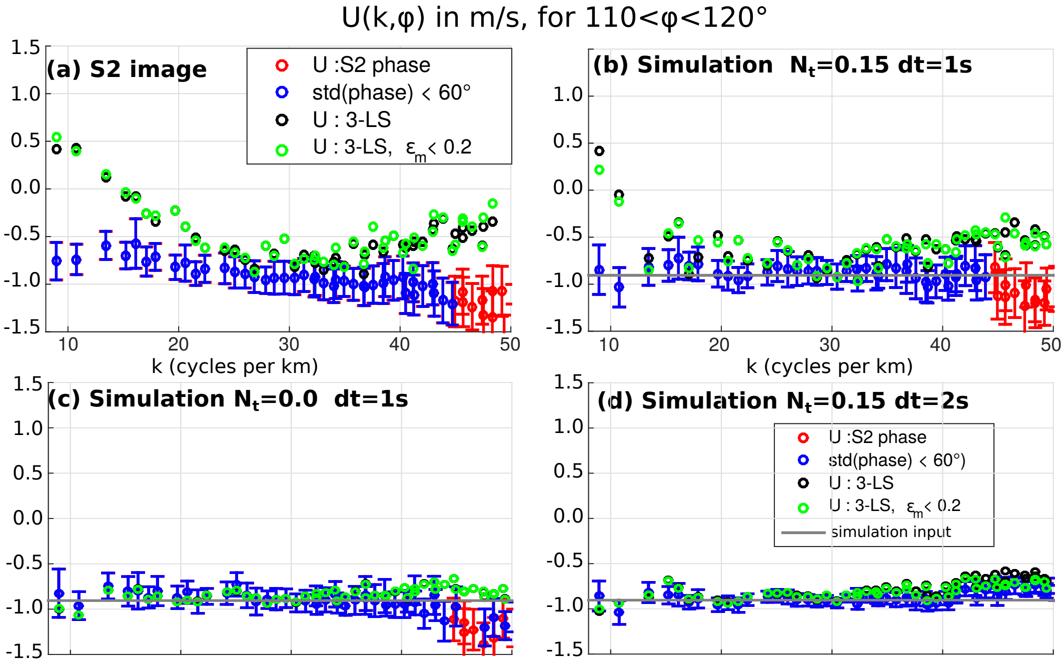


**Figure 10.** Comparison of different current estimates for waves in azimuths 110° to 120° for (a) Sentinel 2 data using bands B04, B03 and B02, and simulated data with the (b) same time lag and similar noise level, or (c) no noise, or (d) a doubled time lag. For the phase difference method (red and blue symbols) the error bars shows the mean value obtained for each spectral component plus or minus one standard deviation divided by the square root of the number of estimates. We have also tested (in green) using a sub-sample of the least-squares, keeping only those with small values of the residual $\varepsilon_m$.

We can think of at least two ways of reducing the phase noise and least square errors. A first possibility may be to reduce the noise of each acquired pixel image, possibly by increasing the integration time to a value larger than several times the life time of specular points, i.e. 10 milliseconds or more. This is clearly not feasible for a push-broom system like the MSI on Sentinel 2 in which the duration of acquisition of each pixel is less than the pixel size (10 m) divided by the ground velocity (7 km/s), i.e. 1.4 ms. However, it is feasible to use a push-frame technique that would repeatedly acquire a full frame at a high frame rate with a large overlap between consecutive frames. A second possibility, without changing spatial resolution, is to increase the time separation of the images so that the mean phase difference is much larger, making random phase differences comparatively smaller. Here we limit the test to a doubling of the time lags in order to avoid the complication of phase ambiguities using both the phase difference method (for which the phase could be shifted by multiples of $2\pi$) or the least squares method (for which several minima may be found). Fig. 10.c,d shows that realistically noisy images with a doubled time lag are preferable to a noise-free image with the same time lag. This is easy to understand in the case of the phase difference method: the larger phase difference makes the random-phase noise a relatively smaller term in the phase difference. The uncertainty on $U$ is inversely proportional to the time difference. This tests also highlight the importance of coherence loss that is not associated to noise and, besides waves in opposing directions, can come from the combination of finite spectral resolution and dispersion.

A first verification of this advantage of larger time lags is provided by using the B12 and B11 band, that are acquired 1.1 s and 0.5 s before B04, which is here 1 s before B02 (this ordering correspond to the even detectors on S2, it is reversed for the odd detectors). Hence combing B12 with B11 and B02, giving a maximum time lag of 2.1 s. However, the spatial resolution of B12 is only 20 m, we have thus averaged B02 over 2 by 2 pixel boxes to provide images at the same resolution, including a 1 m westward shift of B02 to corrected for the error noted above. These results are illustrated in Fig. 11. We

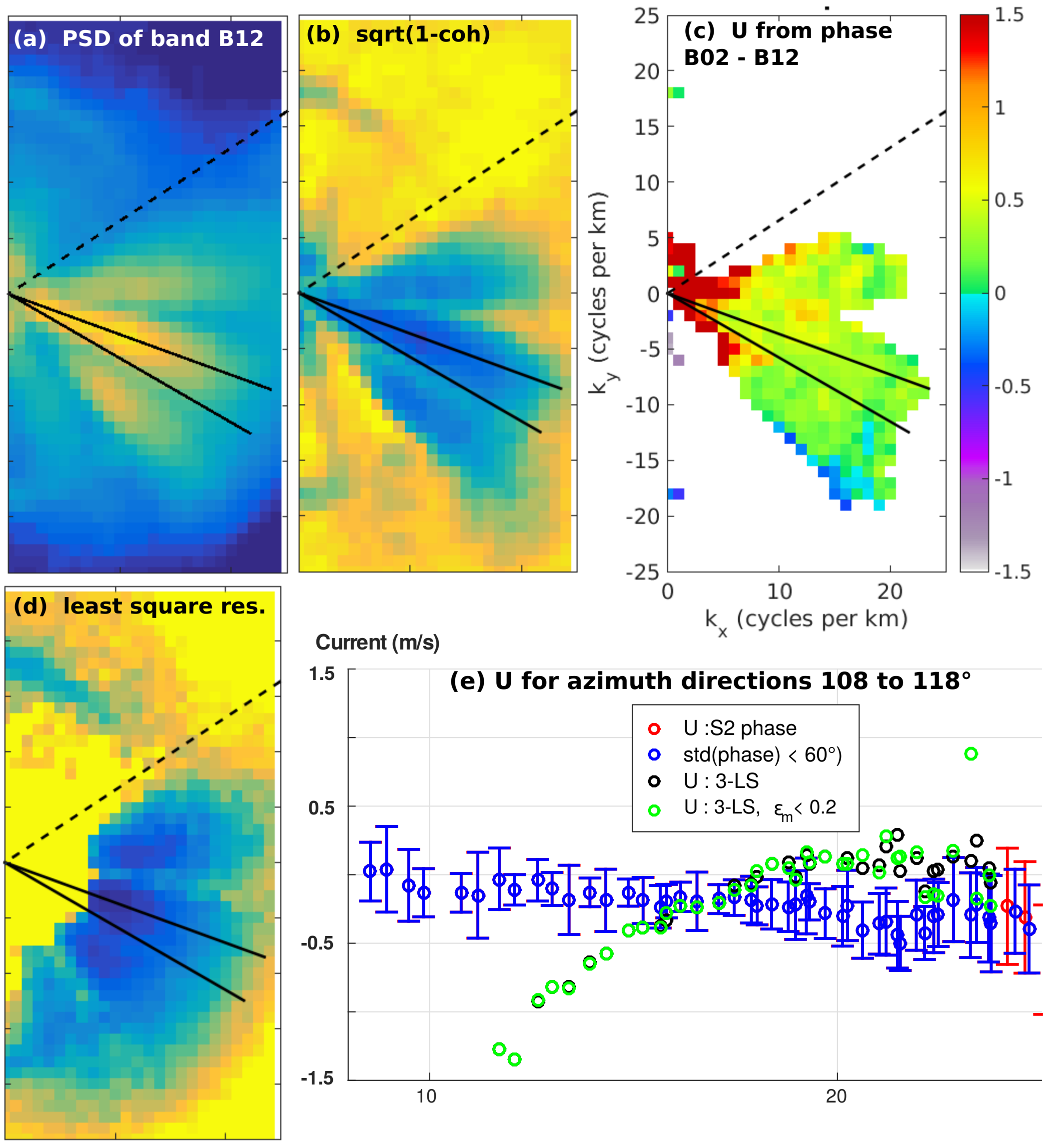


**Figure 11.** Example of results with a larger time lag of 2.1 s but coarser (dx=20m) using B12 and B02 bands. In order to better resolve the longer waves, the spectral analysis was done here with 1 km by 1 km tiles.

first note that the shape of the spectrum, here resolved at higher spectral resolution, shows a 3-lobe structure with minima of the image PSD and coherence for the azimuths 100° and 125°, these are probably due to artefacts of the Level 1-C processing. For the waves in the direction of highest coherence, $108° < \varphi < 118°$, the uncertainty on $U$ obtained in the range of wavenumbers 10 to 20 cpkm is as low as 0.1 m/s in spite of the average of only 64 independent tiles (compared to 256 for Fig. 10.a). Combining all the 25 spectral components available from 10 to 20 cpkm gives an uncertainty of 3.4 cm/s, which we estimated from the mean of the uncertainties divided by the square root of the number of spectral components. Performing the same analysis on 20 m box averages of B03 and B02 gives a 5.8 cm/s uncertainty. It is therefore beneficial to use the largest time lags for estimating the current speed from wavelength between 50 and 100 m. However, we note that the least square method gives rather puzzling results that we do not understand, with a variation of the estimated current as a function of wavenumber that is large and not random.

In the case of the waves shorter than 40 m wavelength, that are only resolved in the 10 m images such as given with bands B02 and B04 with 1 s time lag, the uncertainty of $U$ from the phase difference method for wavenumbers from 30 to 40 cpkm is larger at 4.8 cm/s due to the opposing effects of a lower coherence and a larger number of spectral estimates.

## 4 Discussion: consequences for surface current velocity and shear retrieval

From the consistency of the velocity estimates for all spectral components, and in the particular case of the image analysed in Fig. 2 and 11, we find that Sentinel 2 imagery is capable of providing a velocity precision of the order of 3 to 5 cm/s for spectral ranges of 10 cycles per kilometer. These uncertainties are of the order of the differences in the advection speed of the different spectral components due to a typical vertical current shear in the top 20 m. Mean shear can be very high in the ocean. For example along the equator with differences of the order of 50 cm/s between 1 m and 15 m depth (Sophie Cravatte and Peter Brandt, personal communication 2020) and these should be detectable by Sentinel-2. In contrast, the type of shear shown in Fig. 12 requires detecting 3 cm/s differences between $k = 20$ cpkm and $k = 40$ cpkm, only possible with a reduction of the uncertainty by at least a factor 3, possibly obtained by averaging over at least 24 by 24 km.

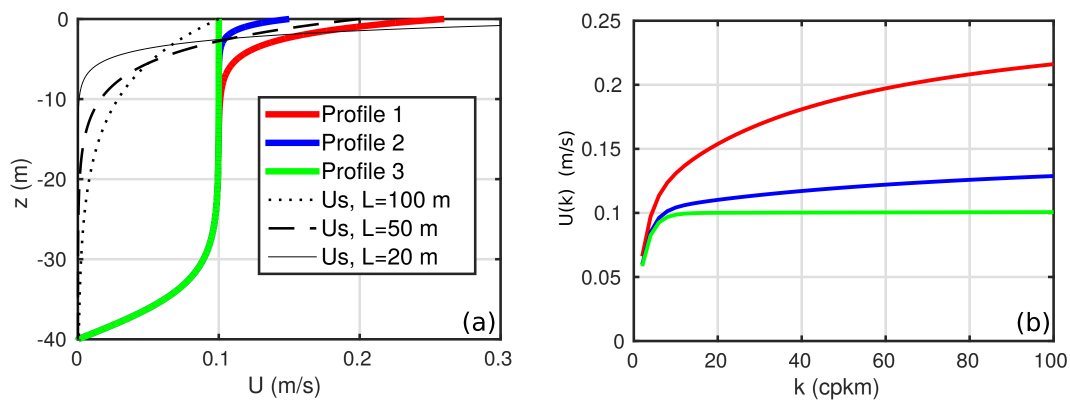


**Figure 12.** (a) Example of typical current profiles of summertime subtropical gyres. Profiles 1 and 2 correspond to figure 1, while profile 3 would be a hypothetical total current profile without Stokes drift. (b) Resulting variation of the effective current $U(k)$ as a function of the wavenumber.

Also, waves are not homogeneous in space, with gradient driven by the horizontal shear of small scale currents (Ardhuin et al., 2017; Quilfen & Chapron, 2019; Villas Bôas et al., 2020). If the shorter waves correlate with currents in a way different from the longer waves, which can be the case at the smallest scales (Suzuki, 2019), what appears like a vertical shear in the difference of phase speed could be the effect of the horizontal shear. Detailed simulations of these effects will be needed to find the order of magnitude of horizontal shear contributions to the mean phase speed difference.

In general, the vertical shear of the current is a priori not sensitive to image co-registration errors because all wavelengths are affected by these errors in the same way, and the shear is associated by a difference in phase speed of the different wave components. We find that a 10 cm/s difference in phase speed between 50 m and 25 m wavelengths (k=20 cpkm and k=40 cpkm) can be detected with Sentinel-2 using data from a 8 km by 8 km region of the ocean. However, such a difference correspond to a fairly large current shear in the top 10 m of the ocean. Resolving weaker and more typical shears would require more sensitive measurements such as provided with larger time lags and higher spatial resolution. Fig. 12.b shows that extending the spectrum to 100 cpkm (10 m wavelengths) would double the difference in velocity that can be detected. Using these shorter components will probably require methods that are less sensitive to the presence of waves in opposite directions, such as the least square method proposed here.

## 5 Conclusions

In order to retrieve a surface current vector and current shear from observed wave dispersion it is necessary to obtain separate and robust estimates of the phase speed of different components of the wave spectrum, with different directions to obtain a current vector, and with different wavelengths to have different sensitivities to different depths.

Although the present work did not define nor demonstrate a full solution method, we have highlighted difficulties associated to the retrieval of phase speed from a small number of ocean surface images using either a phase difference method or a least square fitting of the current velocity and the amplitude of waves in opposing directions. Both methods have complementary advantages and should probably be combined and modified for a successful method. We particularly highlighted how the presence of waves in opposite directions causes error in the phase difference method. In one specific case analyzed here, this is particularly a problem for retrieving phase speeds from waves with wavelengths shorter than 4 times the dominant wind sea. The least square method using 3 or more images is not sensitive to waves in opposing directions, but it provides relatively noisy estimates of the current velocity when applied to Sentinel 2, due to the short time lags (about 1 s). As a result, the least square method may not provide much more useful additional information on the current velocity than the phase difference method. We also note that anomalously low coherence in image pairs may be an indication of the presence of waves in opposite directions, which may have application to the identification of strong microseism or microbarom sources.

However, our simulations show that when applied to other sensors with lower image noise and/or larger time lags, the least square method may allow to use the shortest wave components that are more likely to be associated to high levels of energy propagating in opposing directions. We find that a 2 s time separation and the same pixel noise as Sentinel 2 it should be possible to retrieve reliable phase speeds of shorter waves, all the way to the Nyquist wavelength. In that case it should be viable to reliably estimate the magnitude of waves in opposing directions as quantified by the opposition spectrum introduced in Section 2. Future work will be needed to refine and verify the error model for the two methods and their possible combination.

## Appendix A Image simulator

The first 5 directional moments are converted to a 5-degree resolution directional frequency spectrum using the Maximum Entropy Method (Lygre & Krogstad, 1986). This spectrum is then interpolated onto a regular grid in $(k_x, k_y)$ space to obtain power spectral densities of wave-induced surface elevation with a spectral resolution of 1/16000 cycles per meter, i.e. with a largest wavelength of 16 km, twice as large as the region analyzed. Drawing random phases for each spectral component, the wave power spectral density is used to define complex amplitudes that are inverse-Fourier transformed to generate 8 km square grids of the surface elevation and long wave slopes, $(s_x(x, y, t_i), s_y(x, y, t_i))$, with $x$ and $y$ regularly discretized at 10 m resolution, and $t_i$ the discrete time sampling corresponding to the time of image acquisition.

The input to our image simulator are thus

- the wave spectrum $F(k_x, k_y)$ resolved down to a cut of wavelength of the order of 5 m.
- the direction of the dominant slopes $\varphi_{\mathrm{mss}}$ (which is generally close to the wind direction)
- the mean square slope in that direction $\mathrm{mss}_u$ and the mean square slope in the perpendicular cross-direction $\mathrm{mss}_c$.
- the images bistatic view angles $\beta$ and $\varphi'$ assumed constant for each image.

We note that ideally a full wave spectrum including short gravity waves, e.g. such as parameterized by (Elfouhaily et al., 1997) or modeled by WAVEWATCH III, would also contain the required slope parameters (items 2 and 3 of the above list), but such spectra are not yet realistic enough.

The forward model described in Kudryavtsev et al. (2017a) is used to compute a mean luminance $B_0$ for a locally rough but flat surface, and the local luminance $B(x, y)$ from the same rough surface tilted by the long wave slopes. Detected luminance fluctuations are caused by the true luminance fluctuations caused by the finite number of specular points that contribute to the signal in each pixel (Longuet-Higgins, 1960).

The image pixel value is then taken as the nearest integer of a mean intensity $\langle I \rangle$ times $(1 + n_t)B/B_0$ where $n_t$ is a random white noise of a amplitude $N_t$ that parameterizes the "twinkle" of the sea surface.

The noise of the detector is treated as an additive noise $n_d$, represented as a Gaussian noise of standard deviation $N_d$. For each channel $j$ which corresponds to a time $t_j$ we have the pixel value

$$I_j(x, y) = \mathrm{E}(\langle I \rangle_j \, B(x, y, t_j)/B_0(1 + n_t)), \tag{A1}$$

where the value $\mathrm{E}(x)$ is the largest integer value that is less or equal to $x$. The quantization effect of rounding to an integer pixel value is not very relevant in the present paper with examples that have a relatively bright sea surface. In contrast, the twinkle noise has a very important influence on the estimation of the surface current, as discussed in Sections 2 and 3.

## Appendix B Adaptation of 3-probe least squares method to an unknown current

Let us have $A$ and $B$ the complex amplitudes of the waves propagating in the $\varphi$ direction and the opposite direction $\varphi+\pi$. The system of equations for the 3 measured complex amplitudes $F_1$, $F_2$, $F_3$ at times $t_1 = 0, t_2, t_3$ is, for each spectral component

$(k, \varphi)$, with $U$ the current component in direction $\varphi$, $\sigma = \sqrt{gk}$,

$$\begin{aligned} F_1 &= A + B + N_1 & \text{(B1)} \\ F_2 &= A\mathrm{e}^{-\mathrm{i}(\sigma t_2 + kUt_2)} + B\mathrm{e}^{+\mathrm{i}(\sigma t_2 - kUt_2)} + N_2 & \text{(B2)} \\ F_3 &= A\mathrm{e}^{-\mathrm{i}(\sigma t_3 + kUt_3)} + B\mathrm{e}^{+\mathrm{i}(\sigma t_2 - kUt_2)} + N_3 & \text{(B3)} \\ & & \text{(B4)} \end{aligned}$$

or

$$\begin{aligned} A + B - F_1 &= \varepsilon_1 & \text{(B5)} \\ A\mathrm{e}^{-\mathrm{i}(\sigma t_2 - kUt_2)} + B\mathrm{e}^{+\mathrm{i}(\sigma t_2 + kUt_2)} - F_2 &= \varepsilon_2 & \text{(B6)} \\ A\mathrm{e}^{-\mathrm{i}(\sigma t_3 - kUt_3)} + B\mathrm{e}^{+\mathrm{i}(\sigma t_2 + kUt_2)} - F_3 &= \varepsilon_3 & \text{(B7)} \\ & & \text{(B8)} \end{aligned}$$

and we look for the solution that minimizes the sum of the modulus of $\varepsilon_n$ squared,

$$\sum_n |\varepsilon_n|^2 = \sum_n \left(A\mathrm{e}^{-\mathrm{i}(\sigma t_n - kUt_n)} + B\mathrm{e}^{+\mathrm{i}(\sigma t_n + kUt_n)} - F_n\right)\left(\overline{A}\mathrm{e}^{\mathrm{i}\sigma(t_n - kUt_n)} + \overline{B}\mathrm{e}^{-\mathrm{i}(\sigma t_n + kUt_n)} - \overline{F}_n\right) \tag{B9}$$

where the overbar corresponds to the complex conjugate. Taking derivatives with respect to the real and imaginary parts of $A$ and $B$ and taking derivative with respect to $U$ gives, respectively,

$$\sum_n \mathrm{e}^{-\mathrm{i}(\sigma t_n - kUt_n)}\left(A\mathrm{e}^{-\mathrm{i}(\sigma t_n - kUt_n)} + B\mathrm{e}^{+\mathrm{i}(\sigma t_n + kUt_n)} - F_n\right) = 0 \tag{B10}$$

$$\sum_n \mathrm{e}^{\mathrm{i}(\sigma t_n + kUt_n)}\left(A\mathrm{e}^{-\mathrm{i}(\sigma t_n - kUt_n)} + B\mathrm{e}^{+\mathrm{i}\sigma t_n + kUt_n} - F_n\right) = 0 \tag{B11}$$

$$\sum_n t_n \mathrm{Im}\left[\left(A\mathrm{e}^{-\mathrm{i}(\sigma t_n - kUt_n)} + B\mathrm{e}^{\mathrm{i}(\sigma t_n + kUt_n)}\right)\left(A\mathrm{e}^{-\mathrm{i}(\sigma t_n - kUt_n)} + B\mathrm{e}^{+\mathrm{i}(\sigma t_n + kUt_n)} - F_n\right)\right] = 0, \tag{B12}$$

where $\mathrm{Im}(X)$ is the imaginary part of $X$.

Using $t_1 = 0$, this can be re-arranged as

$$\begin{aligned} \alpha A + \beta B &= \gamma & \text{(B13)} \\ \beta A + \delta B &= \gamma' & \text{(B14)} \\ \mathrm{Im}[t_2\,(\alpha_2 A + \beta_2 B)\cdot(\alpha_2 A + \beta_2 B - F_2) & & \\ +t_3\,(\alpha_3 A + \beta_3 B)\cdot(\alpha_3 A + \beta_3 B - F_3)] &= 0 & \text{(B15)} \end{aligned}$$

where we have defined

$$\begin{aligned} \alpha &= \left[1 + \mathrm{e}^{-\mathrm{i}(2\sigma - 2kU)t_2} + \mathrm{e}^{-\mathrm{i}(2\sigma - 2kU)t_3}\right] & \text{(B16)} \\ \beta &= \left[1 + \mathrm{e}^{\mathrm{i}2kUt_2} + \mathrm{e}^{\mathrm{i}2kUt_3}\right] & \text{(B17)} \\ \gamma &= F_1 + F_2\mathrm{e}^{-\mathrm{i}(\sigma - kU)t_2} + F_3\mathrm{e}^{-\mathrm{i}(\sigma - kU)t_3} & \text{(B18)} \\ \delta &= \left[1 + \mathrm{e}^{2\mathrm{i}(\sigma + kU)t_2} + \mathrm{e}^{2\mathrm{i}(\sigma + kU)t_3}\right] & \text{(B19)} \\ \gamma' &= F_1 + F_2\mathrm{e}^{\mathrm{i}(\sigma + kU)t_2} + F_3\mathrm{e}^{\mathrm{i}(\sigma + kU)t_3} & \text{(B20)} \\ \alpha_2 &= \mathrm{e}^{-\mathrm{i}(\sigma - kU)t_2} & \text{(B21)} \\ \beta_2 &= \mathrm{e}^{\mathrm{i}(\sigma + kU)t_3} & \text{(B22)} \\ \alpha_3 &= \mathrm{e}^{-\mathrm{i}(\sigma - kU)t_3} & \text{(B23)} \\ \beta_3 &= \mathrm{e}^{\mathrm{i}(\sigma + kU)t_3} & \text{(B24)} \end{aligned}$$

We may eliminate $A$ and $B$ from the first 2 equations giving

$$A = (\gamma - \beta B)/\alpha, \tag{B25}$$

and

$$B = (\gamma' - \gamma\beta/\alpha)/(\delta - \beta^2/\alpha). \tag{B26}$$

replacing these expressions for $A$ and $B$ in eq. (B15) gives one equation for $U$,

$$\begin{aligned} f(U, k, \sigma, F_1, F_2, F_3, t_2, t_3) = \mathrm{Im}[\quad & t_2 \quad (\alpha_2 A + \beta_2 B) \times (\alpha_2 A + \beta_2 B - F_2) \\ + \quad & t_3 \quad (\alpha_3 A + \beta_3 B)) \times (\alpha_3 A + \beta_3 B - F_3)] = 0. \end{aligned} \tag{B27}$$

Finding the solution for $f = 0$ gives an estimate of the value of $U$. This operation can be repeated for each Fourier transform (each tile) and each spectral component. Different averaging procedures are discussed in Section 3. In particular we find that the square root of the sum of $|\varepsilon_n|^2$ is linearly correlated to the error on $U$, in particular when the phase differences are large. Finally, this approach is easily extended to more than 3 images.

## Acknowledgments

We acknowledge the use of Copernicus Sentinel 2 data, obtained from the Copernicus Science Hub https://scihub.copernicus.eu. F.A. and M.A. were supported by CNES as part of the SKIM preparation program and ANR grants for ISblue (ANR-17-EURE-0015) LabexMER (ANR-10-LABX-19), and MIMOSA (ANR-14-CE01-0012). M.Yu. was supported by Ministry of Science and Education of the Russian Federation under State Assignment No. 0555-2021-0004 and Russian Science Foundation through the Project No. 21-47-00038. We thank Betrand Chapron for fruitful discussions.

## References

Andrews, D. G., & McIntyre, M. E. (1978). On wave action and its relatives. *J. Fluid Mech.*, *89*, 647–664. (Corrigendum: vol. 95, p. 796)

Ardhuin, F., Chapron, B., Collard, F., Smith, M., Stopa, J., Thomson, J., ... Collins, C. O., III (2017). Measuring ocean waves in sea ice using SAR imagery: A quasi-deterministic approach evaluated with Sentinel-1 and in situ data. *Remote sensing of Environment*, *189*, 211–222. doi: 10.1016/j.rse.2016.11.024

Ardhuin, F., Gualtieri, L., & Stutzmann, E. (2015). How ocean waves rock the earth: two mechanisms explain seismic noise with periods 3 to 300 s. *Geophys. Res. Lett.*, *42*, 765–772. doi: 10.1002/2014GL062782

Ardhuin, F., Marié, L., Rascle, N., Forget, P., & Roland, A. (2009). Observation and estimation of Lagrangian, Stokes and Eulerian currents induced by wind and waves at the sea surface. *J. Phys. Oceanogr.*, *39*(11), 2820–2838. Retrieved from `http://journals.ametsoc.org/doi/pdf/10.1175/2009JPO4169.1` doi: 10.1175/2009JPO4169.1

Ardhuin, F., & Roland, A. (2012). Coastal wave reflection, directional spreading, and seismo-acoustic noise sources. *J. Geophys. Res.*, *117*, C00J20. doi: 10.1029/2011JC007832

Barrick, D. E. (1977). Extraction of wave parameters from measured HF radar sea-echo Doppler spectra. *Radio Science*, *12*, 415–423.

Brekhovskikh, L. M., Goncharov, V. V., Kurtepov, V. M., & Naugolnykh, K. A. (1973). The radiation of infrasound into the atmosphere by surface waves in the ocean. *Izv. Atmos. Ocean. Phys.*, *9*, 899–907 (In the English translation, 511-515.).

Broche, P., de Maistre, J. C., & Forget, P. (1983). Mesure par radar décamétrique cohérent des courants superficiels engendrés par le vent. *Oceanol. Acta*, *6*(1), 43–53.

Campana, J., Terrill, E. J., & Paolo, T. D. (2016). The development of an inversion technique to extract vertical current profiles from X-band radar observations. *J. Atmos. Ocean Technol.*, *33*, 2015–2028. doi: 10.1175/JTECH-D-15-0145.1

Cronin, M. F., Gentemann, C. L., Edson, J., Ueki, I., Bourassa, M., Brown, S., ... Zhang, D. (2019). Air-sea fluxes with a focus on heat and momentum. *Frontiers in Marine Sci.*, *6*, 430.

De Carlo, M., Ardhuin, F., & Pichon, A. L. (2020). Atmospheric infrasound radiation from ocean waves in finite depth: a unified generation theory and application to radiation patterns. *Geophys. J. Int.*, *221*, 569–585. doi: 10.1093/gji/ggaa015

Drusch, M., Del Bello, U., Carlier, S., Colin, O., Fernandez, V., Gascon, F., ... Bargellini, P. (2012). Sentinel-2: Esa's optical high-resolution mission for gmes operational services. *Remote sensing of Environment*, *120*, 25-36. (The Sentinel Missions - New Opportunities for Science) doi: 10.1016/j.rse.2011.11.026

Elfouhaily, T., Chapron, B., Katsaros, K., & Vandemark, D. (1997). A unified directional spectrum for long and short wind-driven waves. *J. Geophys. Res.*, *102*(C7), 15781–15796. doi: 10.1029/97jc00467

Elipot, S., Lumpkin, R., Perez, R. C., Lilly, J. M., Early, J. J., & Sykulski, A. M. (2016). A global surface drifter data set at hourly resolution. *J. Geophys. Res.*, *121*, 2937–2966. doi: 10.1002/2016JC011716

Farrell, W. E., & Munk, W. (2008). What do deep sea pressure fluctuations tell about short surface waves? *Geophys. Res. Lett.*, *35*(7), L19605. doi: 10.1029/2008GL035008

Fedele, F., Benetazzo, A., Gallego, G., Shih, P.-C., Yezzi, A., Barbariol, F., & Ardhuin, F. (2013). Space-time measurements of oceanic sea states. *Ocean Modelling*, *70*, 103–115. doi: 10.1016/j.ocemod.2013.01.001

Guimarães, P. V., Ardhuin, F., Bergamasco, F., Leckler, F., Filipot, J.-F., Shim, J.-S., ... Benetazzo, A. (2020). A data set of sea surface stereo images to resolve space-time wave fields. *Sci. Data*, *7*, 145. doi: 10.1038/s41597-020-0492-95

Hasselmann, K. (1963). A statistical analysis of the generation of microseisms. *Rev. of Geophys.*, *1*(2), 177–210.

Kääb, A., Winsvold, S. H., Altena, B., Nuth, C., Nagler, T., & Wuite, J. (2016). Glacier remote sensing using Sentinel-2. part I: Radiometric and geometric performance, and application to ice velocity. *Radio Science*, *8*, 598. doi: 10.3390/rs807059

Kirincich, A. (2016). Remote sensing of the surface wind field over the coastal ocean via direct calibration of HF radar backscatter power. *J. Atmos. Ocean Technol.*, *33*(7), 1377–1392. doi: 10.1175//JTECH-D-15-0242.1

Kudryavtsev, V., Yurovskaya, M., Chapron, B., Collard, F., & Donlon, C. (2017a). Sun glitter imagery of surface waves. part 1: Directional spectrum retrieval and validation. *J. Geophys. Res.*, *122*. doi: 10.1002/2016JC012425

Kudryavtsev, V., Yurovskaya, M., Chapron, B., Collard, F., & Donlon, C. (2017b). Sun glitter imagery of surface waves. part 2: Waves transformation on ocean currents. *J. Geophys. Res.*, *122*. doi: 10.1002/2016JC012426

Laxague, N. J. M., Özgökmen, T. M., Haus, B. K., Novelli, G., Shcherbina, A., Sutherland, P., ... Molemaker, J. (2018). Observations of near-surface current shear help describe oceanic oil and plastic transport. *Geophys. Res. Lett.*, *44*, 245–249. doi: 10.1002/2017GL075891

Lebedev, K., Yoshinari, H., Maximenko, N. A., & W., H. P. (2007). *Yomaha'07: velocity data assessed from trajectories of argo floats at parking level and at the sea surface* (Tech. Rep. No. 4). Int. Pac. Res. Cent., Univ. Hawaii, Honolulu. Retrieved from `http://apdrc.soest`

.hawaii.edu/projects/yomaha/yomaha07/YoMaHa070612small.pdf ([http://apdrc.soest.hawaii.edu/projects/yomaha/yomaha07/YoMaHa070612small.pdf])

Longuet-Higgins, M. S. (1960). Reflection and refraction at a random moving surface. II. number of specular points in a gaussian surface. *J. Opt. Soc. Am.*, *50*(9), 845–850. doi: 10.1364/JOSA.50.000845

Lumpkin, R., Özgökmen, T., & Centurioni, L. (2017). Advances in the application of surface drifters. *Annu. Rev. Mar. Sci.*, *9*, 6.1–6.23. doi: 10.1146/annurev-marine-010816-060641

Lygre, A., & Krogstad, H. E. (1986). Maximum entropy estimation of the directional distribution in ocean wave spectra. *J. Phys. Oceanogr.*, *16*, 2,052–2,060.

Mansard, E. P. D., & Funke, E. R. (1980). The measurement of incident and reflected spectra using a least squares method. In *Proceedings of international conference on coastal engineering* (Vol. 1). doi: 10.9753/icce.v17.8

Marié, L., Collard, F., Nouguier, F., Pineau-Guillou, L., Hauser, D., Boy, F., ... Ardhuin, F. (2020). Measuring ocean surface velocities with the kuros airborne near-nadir doppler radar: a multi-scale analysis in preparation of the skim mission. *Ocean Sci.*, *16*, 1399–1429. doi: 10.5194/os-16-1399-2020

Maximenko, N., Corradi, P., Law, K. L., Sebille, E. V., Garaba, S. P., Lampitt, R. S., ... Wilcox, C. (2019). Toward the integrated marine debris observing system. *Frontiers in Marine Sci.*, *6*, 447. doi: 10.3389/fmars.2019.00447

Niiler, P. P., & Paduan, J. D. (1995). Wind-driven motions in the Northeast Pacific as measured by Lagrangian drifters. *J. Phys. Oceanogr.*, *25*(11), 2819–2930. Retrieved from http://ams.allenpress.com/archive/1520-0485/25/11/pdf/i1520-0485-25-11-2819

Novelli, G., Guigand, C. M., Cousin, C., Ryan, E. H., Laxague, N. J. M., Dai, H., ... Özgökmen, T. M. (2017). A biodegradable surface drifter for ocean sampling on a massive scale. *J. Atmos. Ocean Technol.*, *34*, 2509–2532. doi: 10.1175/JTECH-D-17-0055.1

Peureux, C., Benetazzo, A., & Ardhuin, F. (2018). Note on the directional properties of meter-scale gravity waves. *Ocean Science*, *14*, 41–52. doi: 10.5194/os-14-41-2018

Quilfen, Y., & Chapron, B. (2019). Ocean surface wave-current signatures from satellite altimeter measurements. *Geophys. Res. Lett.*, *216*, 253-261. doi: 10.1029/2018GL081029

Rio, M.-H., Mulet, S., & Picot, N. (2014). Beyond GOCE for the ocean circulation estimate: Synergetic use of altimetry, gravimetry, and in situ data provides new insight into geostrophic and Ekman currents. *Geophys. Res. Lett.*, *41*, 8918–8925. doi: 10.1002/2014GL061773

Rodríguez, E., Wineteer, A., Perkovic-Martin, D., Gál, T., Stiles, B. W., Niamsuwan, N., & Monje, R. R. (2018). Estimating ocean vector winds and currents using a Ka-band pencil-beam doppler scatterometer. *Remote Sensing*, *4*, 576. doi: 10.3390/rs10040576

Stewart, R. H., & Joy, J. W. (1974). HF radio measurements of surface currents. *Deep Sea Res.*, *21*, 1039–1049.

Suzuki, N. (2019). On the physical mechanisms of the two-way coupling between a surface wave field and a circulation consisting of a roll and streak. *J. Fluid Mech.*, *881*, 906–950. doi: 10.1017/jfm.2019.752

Tyler, G. L., Teague, C. C., Stewart, R. H., Peterson, A. M., Munk, W. H., & Joy, J. W. (1974). Wave directional spectra from synthetic aperture observations of radio scatter. *Deep Sea Res.*, *21*, 989–1016.

Villas Bôas, A. B., Cornuelle, B. D., Mazloff, M. R., Gille, S. T., & Ardhuin, F. (2020). Wave-current interactions at meso and submesoscales: Insights fromidealized numerical simulations. *J. Phys. Oceanogr.*, *in press*. doi: 10.1002/2016JC012413

Wunsch, C., & Ferrari, R. (2009). Ocean circulation kinetic energy:reservoirs, sources, and sinks. *Annu. Rev. Fluid Mech.*, *41*, 253–282. doi: 10.1146/annurev.fluid.40.111406.1021

Young, I. R., Rosenthal, W., & Ziemer, F. (1985). A three-dimensional analysis of marine radar images for the determination of ocean wave directionality and surface currents. *J. Geophys. Res.*, *90*, 1049–1059.

Yurovskaya, M., Kudryavtsev, V., Chapron, B., & Collard, F. (2019). Ocean surface current retrieval from space: The sentinel-2 multispectral capabilities. *Remote sensing of Environment*, *234*, 111468. doi: 10.1016/j.rse.2019.111468

Yurovskaya, M., Rascle, N., Kudryavtsev, V., Chapron, B., Marié, L., & Molemaker, J. (2018). Wave spectrum retrieval from airborne sunglitter images. *Remote sensing of Environment*, *217*, 61–71. doi: 10.1016/j.rse.2018.07.026

Zelt, J. A., & Skjelbreia, J. E. (1993). Estimating incident and reflected wave fields using an arbitrary number of wave gauges. In *Proceedings of 1992 international conference on coastal engineering* (Vol. 1). doi: 10.1061/9780872629332.058